PCCP

ROYAL SOCIETY OF CHEMISTRY

PAPER

View Article Online
View Journal | View Issue





Cite this: *Phys. Chem. Chem. Phys.*, 2023, **25**, 31090

# Computationally directed manipulation of cross-linked covalent organic frameworks for membrane applications†

Alathea E. Davies,[a] Michael J. Wenzel,[a] Cailin L. Brugger,[a] Jordan Johnson,[a] Bruce A. Parkinson,[b] John O. Hoberg[a] and Laura de Sousa Oliveira*[a]

Received 13th September 2023,
Accepted 16th October 2023

DOI: 10.1039/d3cp04452a

rsc.li/pccp

Two-dimensional covalent organic frameworks (2D-COFs) exhibit characteristics ideal for membrane applications, such as high stability, tunability and porosity along with well-ordered nanopores. However, one of the many challenges with fabricating these materials into membranes is that membrane wetting can result in layer swelling. This allows molecules that would be excluded based on pore size to flow around the layers of the COF, resulting in reduced separation. Cross-linking between these layers inhibits swelling to improve the selectivity of these membranes. In this work, computational models were generated for a quinoxaline-based COF cross-linked with oxalyl chloride (OC) and hexafluoroglutaryl chloride (HFG). Enthalpy of formation and cohesive energy calculations from these models show that formation of these COFs is thermodynamically favorable and the resulting materials are stable. The cross-linked COF with HFG was synthesized and characterized with Fourier transform infrared (FTIR) spectroscopy, X-ray diffraction (XRD), thermogravimetric analysis with differential scanning calorimetry (TGA-DSC), and water contact angles. Additionally, these frameworks were fabricated into membranes for permeance testing. The experimental data supports the presence of cross-linking and demonstrates that varying the amount of HFG used in the reaction does not change the amount of cross-linking present. Computational models indicate that varying the cross-linking concentration has a negligible effect on stability and less cross-linking still results in stable materials. This work sheds light on the nature of the cross-linking in these 2D-COFs and their application in membrane technologies.

## 1 Introduction

Two-dimensional covalent organic frameworks (2D-COFs) are highly-ordered materials that exhibit great stability and tunability of their precisely ordered pores, making them ideal for membrane separation applications.[1–5] Recently, a multitude of novel COFs and synthetic approaches have been published.[6–11] Other studies have looked closely at how to optimize current synthetic approaches[6,12] and at what molecular interactions are occurring between the stacked layers.[13] Maintaining the order of these 2D sheets remains a challenge, though, as membrane wetting can result in swelling or dispersion of the COF flakes. As a result, molecules are free to flow around the COF layers rather than through the COF pores, significantly comprimising selectivity. Cross-linking, or chemically "stitching" two layers of a material together, is a promising approach to overcome this challenge. When larger flakes are produced during synthesis, the greater the chance for increased cross-linking. Although cross-linking is not a novel technique in the world of materials science, little work has been done to investigate cross-linking in COFs.[14] In 2021, Kuehl *et al.*[6] published the synthesis of the first quinoxaline-based COF, shown in Fig. 1(a). Cross-linking of this COF with oxalyl chloride $(COCl)_2$ was realized through amide bond formation of the N–H moiety in the pores, as illustrated in Fig. 1(a), where R = $(COCl)_2$. This resulted in improved rejection of the dye Congo Red from 22.1% to 98.3%. This dramatic increase in selectivity was proposed to be from "reduction of the interstitial flow of both solvent and dye, forcing both permeate and retentate through the pores of the COF rather than an interlayer path".[6] Also in 2021, Kong *et al.*[15] published a trimesoyl chloride (TMC) cross-linked COF that was fabricated into a membrane and tested for desalination. The authors varied the amount of TMC during the post-synthetic modification (PSM) from 0 to 0.6 wt%.

[a] *Department of Chemistry, University of Wyoming, Laramie, WY 82071, USA. E-mail: laura.desousaoliveira@uwyo.edu*
[b] *School of Energy Resources, University of Wyoming, Laramie, WY 82071, USA*

† Electronic supplementary information (ESI) available. See DOI: https://doi.org/10.1039/d3cp04452a

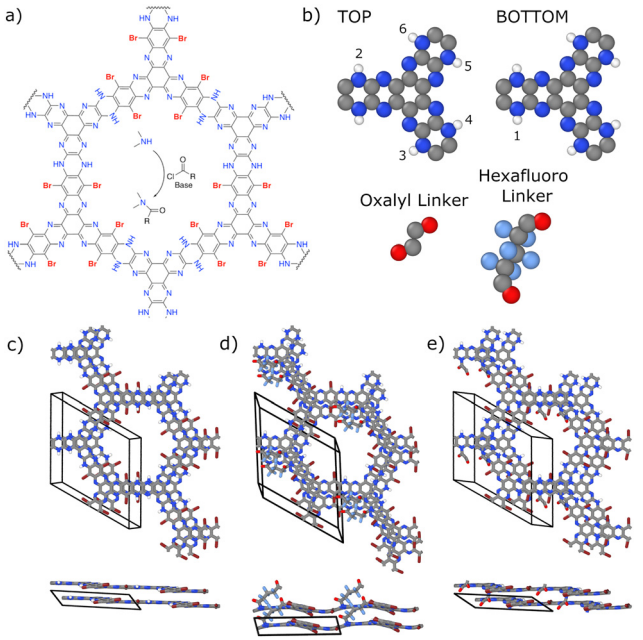


Fig. 1 (a) Reaction mechanism for cross-linking COF-Quin. (b) Cross-linked geometries were generated by assigning the linker, either HFG or OC, to site 1 in the bottom layer. Cross-linking can then occur to one of the numbered sites in the top layer. OC and HFG, as they appear when cross-linked, are also included in (b). Top and side views for COF-Quin (c), COF-Quin cross-linked with HFG (d), and COF-Quin cross-linked with OC (e). The two cross-linked COFs are between sites 1 and 3. The optimized layer spacing is 3.5 Å, 3.8 Å, and 3.3 Å, respectively. Grey spheres are carbon, blue is nitrogen, white is hydrogen, red is oxygen, light blue is fluorine, and maroon is bromine.

The optimum amount of TMC for membrane performance was elucidated through water permeance and salt rejection tests for $Na_2SO_4$, $MgSO_4$, and NaCl. The membrane with 0 wt% demonstrated the highest water flux at 38.12 L $m^{-2}$ $h^{-1}$, but a negligible salt rejection. At 0.2 wt% TMC, the water flux decreased to 2.96 L $m^{-2}$ $h^{-1}$ and the NaCl selectivity increased to 93.3%. Furthermore, the authors were able to improve the water flux to 4.02 L $m^{-2}$ $h^{-1}$ without impacting salt rejection by varying the reaction time of TMC polymerization with the COF. When the concentration of TMC was increased above 0.2 wt%, the salt rejection varied by less than 4%, but the water flux continued to decrease.

Continuing on the work of Kuehl *et al.*,[6] the intent of this study is to provide theoretical insight into the stability of cross-linked COFs. The quinoxaline-based COF, COF-Quin, was cross-linked with hexafluoroglutaryl chloride (HFG) and characterized with Fourier-transform infrared (FTIR) spectroscopy, X-ray diffraction (XRD), and water contact angles, all of which confirmed its incorporation as a cross-linker. *Ab initio* techniques were used to calculate the enthalpies of formation ($\Delta H_f$) and the cohesive energies ($E_{COH}$) of COF-Quin cross-linked with both HFG and oxalyl chloride (OC). $\Delta H_f$ confirms that cross-linking with both molecules is thermodynamically favorable, and $E_{COH}$ supports that the resulting materials are energetically stable. *Ab initio* molecular dynamics simulations of the HFG and OC cross-linked structures were also performed. The MD results corroborate the stability trends seen in the $\Delta H_f$ calculations. Membranes fabricated with COF-Quin demonstrated a decrease in solvent permeance after cross-linking. However, the solvent permeance values did not change for two membranes fabricated with different amounts of HFG. Thermogravimetric analysis with differential scanning calorimetry (TGA-DSC) of these two COFs confirmed that the same amount of degradation occurred, leading to the conclusion that a saturation limit for cross-linking had been achieved in the experimental COFs. In reality, cross-linking is likely not occurring to the same degree as the saturated models. An analysis on the stability of various geometries with decreasing cross-linking concentrations shows that this does not significantly impact the stability of these materials.

## 2 Computational details

### 2.1 Generating cross-linked geometries

The pristine structure of the COF investigated for cross-linking, COF-Quin, is shown in Fig. 1(c), as well as ESI,† Fig. S2a. Cross-linking with both OC and HFG ($ClC(O)(CF_2)_3C(O)Cl$) could occur at any of the N–H bonds within this structure. Theoretical cross-linked structures were exhaustively generated following the numbered sites shown in Fig. 1(b). The linkers, also shown in Fig. 1(b), were connected to a bottom layer at the site numbered 1. Cross-linking could then occur at all other numbered sites in the top layer. Following this methodology, there were 5 initial COF geometries generated for each cross-linking molecule. Fig. 1(d) and (e) display the *ab initio* optimized structures for HFG and OC, respectively, cross-linked between sites 1 and 3.

Geometry and electronic optimizations were carried out using the density functional based tight-binding approach implemented through the package DFTB+.[16] The 3ob-3-1 parameter set was utilized in order to incorporate the accurate third-order expansion of the density functional theory (DFT) total energy and improved Coulomb interactions with hydrogen.[17,18] Lennard-Jones dispersion corrections were also included to account for the non-trivial interlayer van der Waals forces.[19] A 4 × 4 × 4 Monkhorst–Pack scheme[20] was used for *k*-point sampling. Each structure was optimized to a threshold of $1 \times 10^{-5}$ eV for electronic minimization and $1 \times 10^{-4}$ eV $Å^{-1}$ for the atomic forces. The simulation cell parameters for each successfully optimized geometry are provided in ESI,† Table S4. It is noted here that larger cell sizes were simulated in order to vary the cross-linking concentrations. Those cell parameters are also included in ESI,† Table S4.

OC and HFG molecules were optimized inside a box 20 Å × 20 Å × 20 Å, in order to simulate the molecules in isolation. A self-consistent charge (SCC) and forces optimization was conducted *via* DFTB+ with thresholds of $1 \times 10^{-5}$ eV and $1 \times 10^{-4}$ eV $Å^{-1}$ for the charges and forces, respectively. After the molecules had been properly relaxed, the chlorine atoms were removed and a static SCC calculation was performed in order to

calculate the cohesive energy and enthalpy of formation for the molecules as they appear cross-linked in the frameworks. These values are provided in ESI,† Table S1. The .vasp files for all modeled geometries, as well as an example DFTB+ input script, has been uploaded to a Zenodo dataset (see Data availability statement).

### 2.2 Thermodynamic feasibility and structural stability

The thermodynamic favorability of each cross-linked COF geometry was evaluated by calculating the enthalpy of formation, $\Delta H_f$. A more negative enthalpy of formation indicates greater thermodynamic favorability towards forming the geometry in question.[21,22] $\Delta H_f$ was calculated for all cross-linked (XL) geometries and the non-cross-linked (3D) system following eqn (1) and (2), respectively. Although COF-Quin is a 2D-COF, the short-hand notation 3D has been assigned for stacked, non-cross-linked COF-Quin.

$$\Delta H_{f,XL} = \frac{E_{XL} - \sum_{i=1}^{\alpha}\left(N_{i,XL}\frac{E_{i,ref}}{n_{i,ref}}\right)}{M_{XL}} \quad (1)$$

$$\Delta H_{f,3D} = \frac{E_{3D} - \sum_{i=1}^{\alpha}\left(N_{i,3D}\frac{E_{i,ref}}{n_{i,ref}}\right)}{M_{3D}} \quad (2)$$

In eqn (1) and (2), the terms $E_{XL}$ or $E_{3D}$ refer to the total energy of the respective optimized geometries. The summation then occurs over all atom types, $\alpha$, present in the specified geometry. There are 4 atom types in the 3D COF, 5 in the oxalyl chloride XL COFs, and 6 in the hexafluoroglutaryl XL COFs. $N_i$ is the number of atoms of element $i$, in the respective geometry. $E_{i,ref}$ is the total energy of a given element, $i$, in its standard temperature and pressure reference state, which is divided by the number of atoms in that reference state, $n_{i,ref}$. For instance, the reference state for chloride is $Cl_2$. A $Cl_2$ molecule was optimized with DFTB+ to get the total energy, which was then divided by 2. A complete list of reference states and energies for all atom types used in this work is included in ESI,† Table S3, all of which were calculated using DFTB+. The numerators in eqn (1) and (2) are then divided by $M$, which is the total number of atoms in the respective geometry, resulting in the relative enthalpy of formation for each system.

The stability of each structure was analyzed by calculating the cohesive energy, $E_{COH}$, for each cross-linked geometry following eqn (3). The cohesive energy quantifies the amount of energy required to break the material into its individual component atoms. The greater the cohesive energy, the more energy that is required to break the material and, therefore, the more stable the material.[21–25] The cohesive energy for the 3D system can be calculated following the same nomenclature used in eqn (2), however the reference state energy is replaced by the elements gaseous phase atomic energy ($E_{i,atomic}$). This was calculated by isolating an atom of type $i$ in a 20 Å × 20 Å × 20 Å box and optimizing to determine the total energy. The values for each element calculated are also included in ESI,† Table S3.

Following the definition used for $E_{COH}$ as the energy required to break all of the bonds in a material, which must always be a positive value for any stable material, in eqn (3) the total system energy is subtracted from the sum of its individual gas phase atomic energies. Similar to $\Delta H_f$, these values are divided by the total number of atoms in the COF geometry, resulting in the system-relative cohesive energies.

$$E_{COH,XL} = \frac{\sum_{i=1}^{\alpha}\left(N_{i,XL}E_{i,atomic}\right) - E_{XL}}{M_{XL}} \quad (3)$$

The values calculated by the equations above are all relative to each system type. In order to compare the stability of systems with different stoichiometries—*i.e.*, to compare how the different cross-linking moieties affect the stability of the framework—the following equations have been derived for $\Delta H_f$ and $E_{COH}$.

$$\Delta H_f = \frac{\left[E_{XL} - \sum_{i=1}^{\alpha}\left(N_{i,XL}\frac{E_{i,ref}}{n_{i,ref}}\right)\right] - \left[E_{LM} - \sum_{i=1}^{\alpha}\left(N_{i,LM}\frac{E_{i,ref}}{n_{i,ref}}\right)\right]}{M_{XL} - M_{LM}} \quad (4)$$

$$E_{COH} = \frac{\left[\sum_{i=1}^{\alpha}\left(N_{i,XL}E_{i,atomic}\right) - E_{XL}\right] - \left[\sum_{i=1}^{\alpha}\left(N_{i,LM}E_{i,atomic}\right) - E_{LM}\right]}{M_{XL} - M_{LM}} \quad (5)$$

Eqn (4) calculates the enthalpy of formation of the COF framework without energetic contributions from the cross-linking moiety. This equation is very similar to eqn (1), however, the values from the linking moiety, LM, are subtracted from the values of the XL COF. This is also performed in eqn (5) for calculating the cohesive energy of the COF framework without energetic contributions from the linking moiety. Using both of these equations, we are able to compare how stable the COF-Quin framework is made by the two different linking moieties.

All $\Delta H_f$ and $E_{COH}$ values calculated from the equations provided in this section are visualized in Fig. 3 and discussed in Section 3.1. Numerical values for $\Delta H_f$ and $E_{COH}$ calculated by eqn (1)–(3) are provided in ESI,† Table S1. The values calculated from eqn (4) and (5) are provided in ESI,† Table S2. An Excel spreadsheet with the atom number densities and DFTB+ total energy values for all systems has been included in the aforementioned Zenodo dataset, along with a Python script for calculating enthalpy of formation and cohesive energy (see Data availability statement).

### 2.3 *Ab initio* molecular dynamics

*Ab initio* equilibrium molecular dynamics (MD) simulations were performed at 300 K and 600 K to further evaluate the thermal stability of the geometries. A 2 × 2 × 5 supercell was tested for six geometries: COF-$Quin_{3D}$, COF-XL,HFG at sites 1-2, 1-3 and 1-4, and COF-XL,OC at sites 1-3 and 1-4. MD simulations were also conducted using the package DFTB+,[16] and all of the corrections previously mentioned. Both temperatures

 

were simulated for 10 ps. A timestep of 1 fs was used. The first 2 ps of each simulation were conducted in the isothermal–isobaric (*NPT*) ensemble using the Nosé–Hoover thermostat[26] and Berendsen barostat[27] at 1 atm. The remaining 8 ps were simulated under the microcanonical (*NVE*) ensemble. The software package OVITO was used for visualizations.[28] The results from the MD simulations are discussed at the end of Section 3.1.

# 3 Results and discussion

## 3.1 COF Formation and stability

COF-Quin was synthesized as described by Kuehl *et al.*,[6] followed by cross-linking with HFG. As reported previously, the presence of C–F bonds was confirmed *via* FTIR (see ESI,† Fig. S1). Fig. 2 illustrates the XRD for COF-XL,HFG (orange) with an insert from Kuehl *et al.*[6] of the powder X-ray diffraction (PXRD) pattern for the non-cross-linked quinoxaline COF. In the experimental COF-Quin$_{3D}$ pattern, there is a peak representing interlayer separation at 27°. In the cross-linked XRD, the broad peak between 12–35° is likely partially due to the cross-linking moiety increasing the layer separation. During the PSM, layers closer to the surface of the COF are able to spread apart more, accommodating cross-linking geometries and interlayer separations closer to the simulated HFG 1-3, 1-4, 1-5 and 1-6 structures (ESI,† Table S1). However, intercalation into the inner most COF layers becomes more difficult and thus, these layers remain unaffected. This broad pattern in the XRD indicates a disordered material with a range of layer separations thus supporting the presence of cross-linking. Additionally, the water contact angle images in ESI,† Fig. S3 support this observation.

The five initial cross-linking structures with both OC and HFG were optimized *via* DFTB+. All five structures cross-linked with HFG converged successfully. However, only two structures cross-linked with OC converged successfully and without degradation of the linker. The two successful sites were 1-3 and 1-4. In Fig. 3(a), $E_{COH}$ (light/dark blue) and $\Delta H_f$ (orange/red) for each of these structures are shown as bar plots. The two darker blue (red) bars indicate the values for the two OC cross-linked geometries, whereas the five light blue (orange) bars represent the values for the five HFG cross-linked geometries. The dark blue (red) dashed lines indicate $E_{COH}$ ($\Delta H_f$) for COF-Quin$_{3D}$. Note that in Fig. 3, the right-hand axis for $\Delta H_f$ has been inverted for ease of plotting and interpretation of the results;

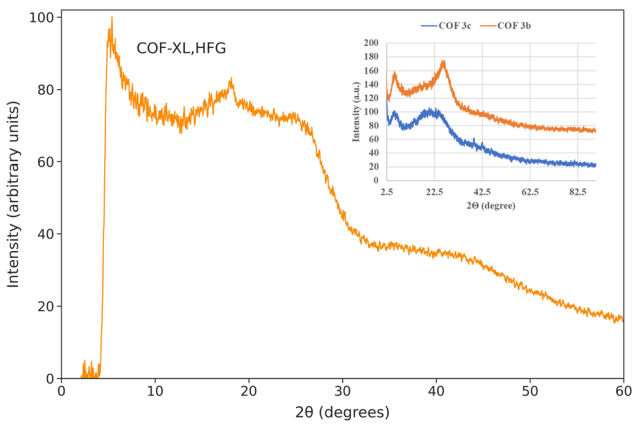


Fig. 2 XRD pattern for COF-XL,HFG with an insert showing the powder X-ray diffraction (PXRD) pattern for COF-Quin (orange), reprinted with the permission of Kuehl *et al.*[6] The blue XRD pattern from this insert is for a propargylic acid functionalized quinoxaline COF synthesized by Kuehl *et al.*[6] Simulated XRD patterns for HFG cross-linked geometries are illustrated in ESI,† Fig. S4.

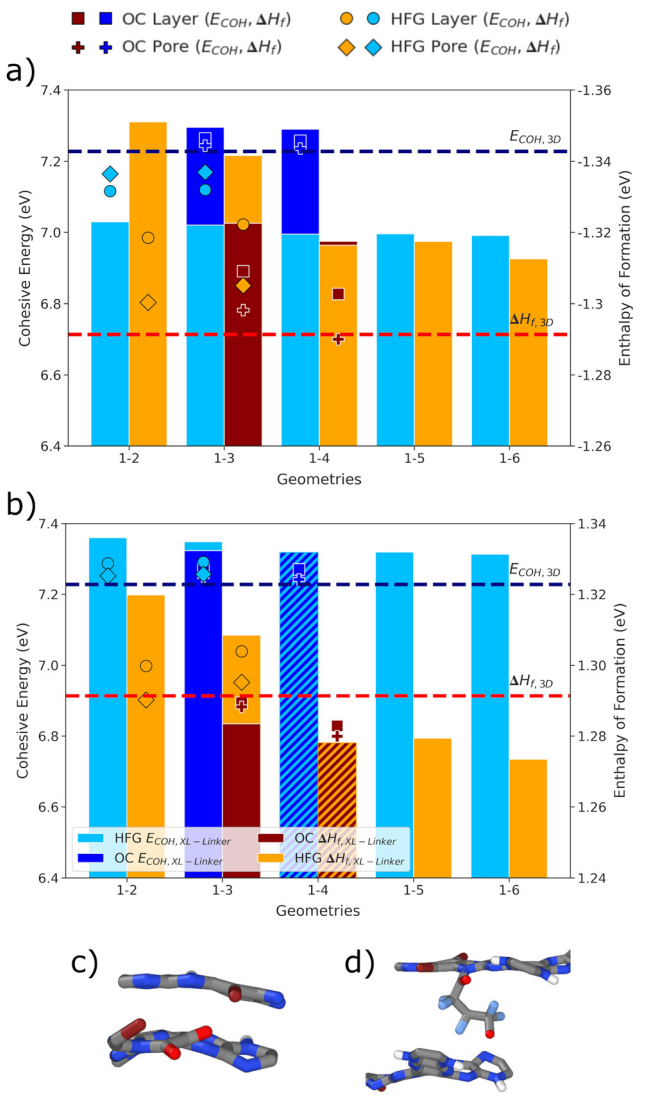


Fig. 3 $E_{COH}$ (left-hand *y*-axis) and $\Delta H_f$ (right-hand *y*-axis) for each cross-linked structure. There are five light blue/orange bars for each HFG structure and two dark blue/red bars for the two OC structures at sites 1-3 and 1-4. The bars represent "saturated" cross-linking. The points correspond to "distributed" geometries as labeled in the legend at the top of the figure. The dark blue (red) dashed line is for $E_{COH}$ ($\Delta H_f$) for COF-Quin$_{3D}$. Please note that the right-hand *y*-axis for $\Delta H_f$ has been inverted for ease of plotting. (a) The total $E_{COH}$ and $\Delta H_f$ calculated by eqn (3) and (1), respectively. (b) Similarly, the framework energies calculated from eqn (5) and (4). Images from the molecular dynamics of OC 1-3 (c) and HFG 1-4 (d) at 600 K where the linking moiety breaks apart from the framework.

stability and favorability are in this way represented by higher values. The values for the data plotted in Fig. 3 are provided in ESI,† Tables S1 and S2.

In the case of both cross-linked frameworks, shown in Fig. 3(a), the negative $\Delta H_f$ indicates that the formation of these structures is thermodynamically favorable. In fact, $\Delta H_f$ is more negative for all cross-linked structures than COF-Quin$_{3D}$, indicating that in the presence of OC and HFG, cross-linking of the quinoxaline COF is very favorable. Similarly, the large positive values of $E_{COH}$ indicate that these structures are very stable and have strong intramolecular bonds. It is significant to note that of the starting five theoretical cross-linking sites for HFG, all five sites successfully converged while only two of the original five geometries converged for OC. It is likely due to increased steric hindrance that the other three geometries did not converge. As OC is much shorter in length than HFG (a two-carbon *versus* five-carbon chain), it would be unable to increase interlayer separation and maintain cross-linking in order to reduce sterics. HFG, however, has the ability to stretch and increase layer separation in order to reduce any sterics while maintaining cross-linking between those layers. The 1-2 and 1-3 cross-linked HFG structures have an interlayer separation of 3.9 Å and 3.8 Å, respectively, while the other three geometries have interlayer separations from 8.53–8.76 Å. One possible explanation for the lower (more favorable) enthalpy of formation for sites 1-2 and 1-3, is that the hexafluoroglutaryl linker is able to lay relatively flat across the space of the open pore, likely reducing steric hindrance and leading to the much smaller interlayer separation, which also correlates to stronger dispersion forces between the framework layers. The location of the bromine atoms in the other three geometries do not appear to allow for the linker to lay flat, thereby forcing the linker into a more upright position to reduce repulsion and steric hindrance.

Fig. 3(b) shows $E_{COH}$ and $\Delta H_f$ calculated by eqn (5) and (4). The values are plotted and labeled in the same fashion as Fig. 3(a). While Fig. 3(a) shows a stronger $E_{COH}$ for the two OC sites than COF-Quin$_{3D}$ and the five HFG sites, Fig. 3(b) shows that $E_{COH}$ of the framework is almost equal regardless of the linking moiety used. Additionally, $E_{COH}$ of the cross-linked structures compares favorably to that of COF-Quin$_{3D}$. The trend in $\Delta H_f$ here for the cross-linked geometries is very similar to the trend seen in Fig. 3(a). However, after the linking energies have been subtracted only HFG sites 1-2 and 1-3 are more thermodynamically favorable than COF-Quin$_{3D}$, while all other HFG and OC sites are less favorable. This is most likely due to the layer offset and separations of these structures being unattainable without the presence of cross-linking moieties. The OC geometries are held much closer together (3.29 Å and 3.17 Å) than COF-Quin$_{3D}$ would naturally prefer (3.45 Å). Alternatively, HFG 1-4, 1-5, and 1-6 have very large layer separations (8.53–8.76 Å) that are very energetically unfavorable for COF-Quin$_{3D}$. In order to achieve these specific layer separations, cross-linking is required. The effect of cross-linking concentration on the stability of the framework is discussed in Section 3.3.

*Ab initio* MD simulations were performed for COF-Quin$_{3D}$, as well as for HFG (1-2, 1-3, and 1-4) and OC (1-3 and 1-4). Over the 10 ps performed for each geometry at 300 K, there was very little fluctuation in the bond lengths. However, at 600 K, only COF-Quin$_{3D}$ and HFG 1-2 completed the full 10 ps simulation. All other structures saw a breaking of one or two cross-linking moieties from the framework, a visual example of which is provided in Fig. 3(c) and (d) for OC 1-3 and HFG 1-4, respectively. As there are twenty total linkers in each $2 \times 2 \times 5$ supercell, the breaking of one or two does not cause a noticeable effect on the average bond lengths provided in ESI,† Table S5. The reason that HFG 1-2 retained cross-linking is likely due to the favorable combination of its $E_{COH}$ and $\Delta H_f$.

Many of the molecular dynamics studies on COFs, particularly with respect to COFs intended for membrane separation applications, use classical MD, which rely on the accuracy of the forcefields that are being employed.[29–32] Although *ab initio* MD is limited by system size and simulation time, the accuracy of the calculations is not as closely tied to the accuracy of selected parameters (and choice of interatomic potential). The aforementioned studies also assume rigidity in the COF material in order to increase the speed of the simulations. However, recent work suggests that vibrational coupling can occur between fluids and 2D materials, and that this coupling can significantly enhance the fluid permeance.[33,34] No rigidity was enforced for the *ab initio* MD simulations in this work, allowing the materials to fully vibrate as a function of temperature.

### 3.2 Membrane testing

Three variations of COF-Quin were synthesized and fabricated into a membrane for permeance testing by loading pure COF onto an anodic aluminum oxide (AAO) support, the methods for which are detailed in the (ESI†).[35] COF-Quin$_{CF3}$ is a fluorinated version of COF-Quin, as reported previously,[6] a visual representation of which is given in ESI,† Fig. S2b. COF-XL,HFG and COF-XXL,HFG are cross-linked COFs reacted with an equivalent and excess amount of HFG, respectively. As previously reported, cross-linking with OC produced dramatic results in the rejection of dyes with an improvement from 22% to 99% rejection with two different dyes. This selectivity increase and the associated permeance decrease in the cross-linked membrane is a consequence of preventing interstitial flow of both water and dye, forcing both permeate and retentate through the pores of the COF rather than an interlayer path.[6] In moving from dye separation to the more difficult solvent separations, a permeance decrease is still observed. The permeance data shown in Fig. 4(a) indicates that the use of HFG cross-linking only decreases permeance slightly in polar solvents and more significantly with less polar solvents such as acetone and THF. However, increasing the amount of cross-linking reagent (XL in green *versus* XXL orange) has no meaningful effect on solvent permeance, presumably due to a saturation limit for cross-linking with HFG in COF-Quin. This latter aspect is observed with the solvents EtOH, DMF, MeOH and THF in which all permeance data are within error limits of each other. Only in the case of acetone is there any noticeable difference in separations.

The amount of HFG cross-linking was investigated further *via* TGA-DSC, Fig. 4(b). A loss of water is observed in

 

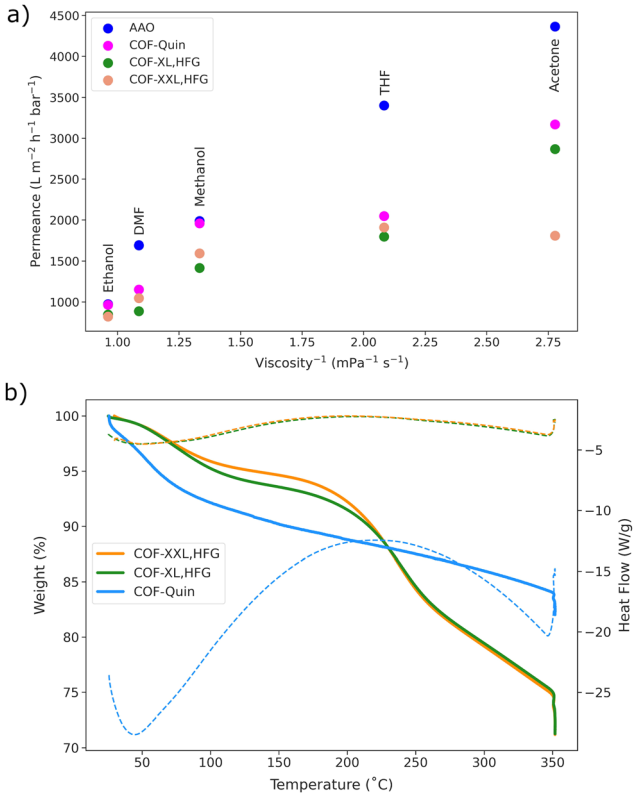


Fig. 4 Membrane permeance testing for COF-Quin, COF-XL,HFG, and COF-XXL,HFG, as well as a blank AAO support (a). The solvents used in permeance tests are detailed in ESI,† Table S5. TGA-DSC (b) for COF-Quin (blue), COF-XL,HFG (green) and COF-XXL,HFG (orange). The weight percent (left-hand *y*-axis) is plotted in solid lines while the heat flow (right-hand *y*-axis) is plotted in dashed lines.

both cross-linked and non-cross-linked COFs up to 100 °C, with nearly identical amounts of degradation seen for both COF-XL,HFG (green) and COF-XXL,HFG (orange). Noticeably, COF-Quin appears to be more highly hydrated likely due to the increased flake expansion. The second noticeable loss, beginning at 200 °C, is only observed in the cross-linked COFs, and thus is likely due to loss of the linking moiety. Given that both COF-XL and COF-XXL are identical in weight loss, it appears that varying the amount of cross-linking reagent included in the PSM reaction does not lead to additional cross-linking. It is also noted that the TGA-DSC data for COF-Quin (blue) in Fig. 4(b) does not show the same degradation, further supporting that cross-linking *via* HFG is present in COF-XL, HFG and COF-XXL, HFG. The TGA-DSC results also agree with the MD which show that degradation would have happened at 600 K but not 300 K.

### 3.3 Cross-linking concentrations

In order to investigate the effect of different concentrations of cross-linking on the COF stability, two additional geometries for both OC and HFG were modeled. The geometries discussed in previous sections were "saturated" with cross-linking and contained one linker in each pore per layer, as shown in Fig. 5(a). The two "distributed" geometries include a

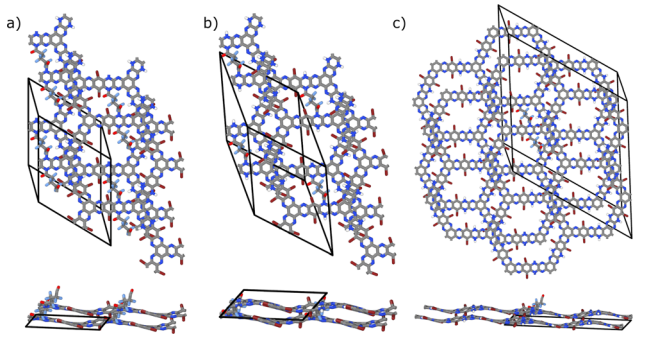


Fig. 5 Different concentrations of cross-linking molecules were simulated to investigate the effect it would have on the framework stability. Top and side views of saturated cross-linking with hexafluoroglutaryl chloride (a), hexafluoroglutaryl chloride in every pore and every other layer ("layers", (b)), and hexafluoroglutaryl chloride in every other pore and every layer ("pores", (c)). In a 2 × 2 × 2 supercell, there are 8, 4 and 2 linkers present for saturated, "layers", and "pore" geometry, respectively.

cross-linker in every pore and every other layer, called "layers" in Fig. 3, and a cross-linker in every other pore and every layer, called "pore" in Fig. 3. A visual representation for these geometries with HFG is given in Fig. 5. Images for these geometries with OC are given in ESI,† Fig. S5.

The points plotted in Fig. 3 represent each of these distributed geometries with colors consistent to their respective linker. In both plots in Fig. 3, $E_{COH}$ and $\Delta H_f$ trend towards COF-Quin$_{3D}$, the non-cross-linked COF. As cross-linking moieties are removed, the structure has a greater percentage of the framework that is identical to COF-Quin$_{3D}$. In other words, the limit of $E_{COH}$ and $\Delta H_f$ as a function of linking moiety concentration is the respective values for COF-Quin$_{3D}$. As COF-Quin$_{3D}$ is still a stable framework, evidenced by the positive $E_{COH}$ and the negative $\Delta H_f$, decreasing the linking concentration has no significant effect on the framework stability.

It is highly unlikely that the modeled "saturation", where cross-linking occurs in every pore and every layer, is the saturated cross-linking that is seen in the experimental COFs due to the nature of post-synthetic modifications. It is also very challenging to quantify the amount of cross-linking that is occurring within the experimental COFs. Based on stability calculations and the broadening of the XRD peak for layer spacing, it is likely that a distribution of (the modeled) cross-linking sites and concentrations are occurring in reality.

## 4 Conclusions

The enthalpy of formation and cohesive energy calculations from modeled cross-linked COFs indicate that cross-linking with both oxalyl chloride and hexafluoroglutaryl chloride is thermodynamically favourable and results in stable cross-linked COFs. In order to determine which cross-linking molecule resulted in a more stable framework, the energy contributions from each of the cross-linking molecules were subtracted from the total values of the cross-linked materials. Based on cohesive energy values, it was concluded that cross-linking with either hexafluoroglutaryl

chloride or oxalyl chloride increased the intramolecular bond strength of the framework by an equal amount beyond that of the non-cross-linked COF, thereby increasing the stability of the framework upon cross-linking. Hexafluoroglutaryl chloride, however, is a more favorable cross-linking moiety based on enthalpy of formation values for the framework and the fact that it is a longer molecule than oxalyl chloride, thereby resulting in many more possible stable cross-linked structures than oxalyl chloride. *Ab inito* molecular dynamics at 600 K for multiple hexafluoroglutaryl and oxalyl chloride structures agreed with the trends in stability from enthalpy of formation calculations given that the most favorable enthalpy of formation value corresponded to the only cross-linked structure, HFG 1-2, that did not degrade at 600 K.

Membranes fabricated from these COFs exhibit a decrease in permeance after cross-linking by varying degrees for all solvents tested. COF-Quin was also reacted with two different amounts of hexafluoroglutaryl chloride. For these two COFs, there is a marginal change in permeance and the same amount of degradation is seen in both TGA-DSC figures. It can be concluded from this data that cross-linking *via* hexafluoroglutaryl chloride has reached a certain level of saturation. Additional *ab initio* models of the cross-linked COFs were conducted to investigate the effect of limited cross-linking on the material stability. It was concluded from these calculations that decreasing the amount of cross-linking moieties results in a framework that resembles, both in structure and stability, the non-cross-linked COF, which is still deemed a stable framework from cohesive energy and enthalpy of formation calculations. At this time, though, it is difficult to assess what amount of hexafluoroglutaryl chloride cross-linking is occurring in the material and to correlate that to one of the modeled structures. More likely, a combination of the cross-linking sites and concentrations are occurring in reality as evidenced by the broad XRD peak.

Very limited work has been done to explore cross-linking between 2D-COF layers, but the published work indicates that cross-linking significantly improves membrane selectivity. This work has provided insight into the stability of covalently cross-linked 2D-COFs, thereby supporting the continued research into their use for membrane separation processes.

## Data availability

The structure files for all modeled geometries, as well as an example DFTB+ input script and Python script for calculating stability values, are available on Zenodo: A. E. Davies, M. J. Wenzel, C. L. Brugger, J. Johnson, B. A. Parkinson, J. O. Hoberg and L. de Sousa Oliveira, 2023, Zenodo, DOI: **10.5281/zenodo.10065153**.

## Author contributions

Alathea E. Davies: investigation, data curation, methodology, visualization, writing – original draft, and writing – review and editing. Michael J. Wenzel: investigation, visualization, and writing – original draft. Cailin L. Brugger: investigation. Jordan Johnson: investigation. Bruce A. Parkinson: conceptualization, funding acquisition, resources, supervision, and writing – review and editing. John O. Hoberg: conceptualization, data curation, funding acquisition, methodology, project administration, resources, supervision, visualization, writing – original draft, and writing – review and editing. Laura de Sousa Oliveira: conceptualization, data curation, funding acquisition, methodology, project administration, resources, supervision, visualization, writing – original draft, and writing – review and editing.

## Conflicts of interest

There are no conflicts to declare.

## Acknowledgements

The authors acknowledge generous support from NSF-DMREF grant #2118592, DOE-BES grant #DE-SC0020100, and NSF-REU grant #2051148. The authors would also like to acknowledge the use of computational resources at the NCAR-Wyoming Supercomputing Center provided by the National Science Foundation and the State of Wyoming, and supported by NCAR's Computational and Information Systems Laboratory (Project WYOM0145),[36] and the Advanced Research Computing Center, Beartooth Computing Environment at the University of Wyoming.[37]

## Notes and references

1 A. P. Côté, A. I. Benin, N. W. Ockwig, M. O'Keeffe, A. J. Matzger and O. M. Yaghi, *Science*, 2005, **310**, 1166–1170.
2 L. Lin, J. Choi and J. C. Grossman, *Chem. Commun.*, 2015, **51**, 14921–14924.
3 S. Yuan, X. Li, J. Zhu, G. Zhang, P. V. Puyvelde and B. van der Bruggen, *Chem. Soc. Rev.*, 2019, **48**, 2665–2681.
4 J. Shen, J. Yuan, B. Shi, X. You, R. Ding, T. Zhang, Y. Zhang, J. Guan, M. Long, Y. Zheng, R. Zhang, H. Wu and Z. Jiang, *J. Mater. Chem. A*, 2021, **9**, 23178–23187.
5 P. H. H. Duong, Y. K. Shin, V. A. Kuehl, M. M. Afroz, J. O. Hoberg, B. A. Parkinson, A. C. T. van Duin and K. D. Li-Oakey, *Sep. Purif. Technol.*, 2022, **282**, 120028.
6 V. A. Kuehl, P. H. H. Duong, D. Sadrieva, S. A. Amin, Y. She, K. D. Li-Oakey, J. L. Yarger, B. A. Parkinson and J. O. Hoberg, *ACS Appl. Mater. Interfaces*, 2021, **13**, 37494–37499.
7 C. Liu, Y. Jiang, A. Nalaparaju, J. Jiang and A. Huang, *J. Mater. Chem. A*, 2019, **7**, 24205–24210.
8 M. A. Solomos, F. J. Claire and T. J. Kempa, *J. Mater. Chem. A*, 2019, **7**, 23537–23562.
9 V. Spaulding, K. Zosel, P. H. H. Duong, K. D. Li-Oakey, B. A. Parkinson, D. A. Gomez-Guadron and J. O. Hoberg, *Mater. Adv.*, 2021, **2**, 3362.

 

10 P. H. H. Duong, V. A. Kuehl, B. Mastorovich, J. O. Hoberg, B. A. Parkinson and K. D. Li-Oakey, *J. Membr. Sci.*, 2019, **574**, 338–348.
11 V. A. Kuehl, J. Yin, P. H. H. Duong, B. Mastorovich, B. Newell, K. D. Li-Oakey, B. A. Parkinson and J. O. Hoberg, *J. Am. Chem. Soc.*, 2018, **140**, 18200–18207.
12 J. Brophy, K. Summerfield, J. Yin, J. Kephart, J. T. Stecher, J. Adams, T. Yanase, J. Brant, K. D. Li-Oakey, J. O. Hoberg and B. A. Parkinson, *Materials*, 2021, **14**, 71.
13 P. H. H. Duong, Y. K. Shin, V. A. Kuehl, M. M. A. J. O. Hoberg, B. Parkinson, A. C. T. van Duin and K. D. Li-Oakey, *ACS Appl. Mater. Interfaces*, 2021, **13**, 42164–42175.
14 J. L. Segura, S. Royuela and M. Mar Ramos, *Chem. Soc. Rev.*, 2019, **48**, 3903–3945.
15 F. Kong, L. Yue, Z. Yang, G. Sun and J. Chen, *ACS Appl. Mater. Interfaces*, 2021, **13**, 21379–21389.
16 B. Hourahine and B. Aradi, *et al.*, *J. Chem. Phys.*, 2020, **152**, 124101.
17 M. Gaus, Q. Cui and M. Elstner, *J. Chem. Theory Comput.*, 2011, **7**, 931–948.
18 M. Gaus, A. Goez and M. Elstner, *J. Chem. Theory Comput.*, 2013, **9**, 338–354.
19 A. K. Rappe, C. J. Casewit, K. S. Colwell, W. A. Goddard III and W. M. Skiff, *J. Am. Chem. Soc.*, 1992, **114**, 10024–10035.
20 H. J. Monkhorst and J. D. Pack, *Phys. Rev. B: Solid State*, 1976, **13**, 5188–5192.
21 S. Ghosh and J. K. Singh, *Int. J. Hydrogen Energy*, 2020, **44**, 1782–1796.
22 J. Wang, B. Li and C.-H. Zhang, *Appl. Phys. A: Mater. Sci. Process.*, 2021, **127**, 637.
23 J. Cajzl, P. Nekvindova, A. Mackova, M. Varga and A. Kromka, *Phys. Chem. Chem. Phys.*, 2022, **24**, 19052–19072.
24 I. Perez, *Phys. Chem. Chem. Phys.*, 2023, **25**, 1476–1503.
25 V. K. Yadav, S. H. Mir, V. Mishra, T. G. Gopakumar and J. K. Singh, *Phys. Chem. Chem. Phys.*, 2020, **22**, 21360–21368.
26 G. J. Martyna, M. E. Tuckerman, D. J. Tobias and M. L. Klein, *Mol. Phys.*, 1996, **87**(5), 1117–1157.
27 H. J. C. Berendsen, J. P. M. Postma, W. F. van Gunsteren, A. DiNola and J. R. Haak, *J. Chem. Phys.*, 1984, **81**, 3684–3690.
28 A. Stukowski, *Mater. Sci. Eng.*, 2010, **18**, 15012.
29 K. Zhang, Z. He, K. M. Gupta and J. Jiang, *Environ. Sci.: Water Res. Technol.*, 2017, **3**, 735–743.
30 W. Zhou, M. Wei, X. Zhang, F. Xu and Y. Wang, *ACS Appl. Mater. Interfaces*, 2019, **11**, 16847–16854.
31 Y. Zhang, T. Fang, Q. Hou, Z. Li and Y. Yan, *Phys. Chem. Chem. Phys.*, 2020, **22**, 16978–16984.
32 X. Zhu, B. Ma, Y. Ai, L. Zhang, X. Wang, L. Lian and J. Shen, *Microporous Mesoporous Mater.*, 2023, **349**, 112417.
33 Y. Noh and N. R. Aluru, *Nano Lett.*, 2022, **22**, 419–425.
34 Z. L. Terranova and F. Paesani, *Phys. Chem. Chem. Phys.*, 2016, **18**, 8196–8204.
35 A. M. Tandel, W. Guo, K. Bye, L. Huang, M. Galizia and H. Lin, *Mater. Adv.*, 2021, **2**, 4574–4603.
36 Computational and Information Systems Laboratory, Cheyenne: HPE/SGI ICE XA System (NCAR Community Computing). Boulder, CO: National Center for Atmospheric Research.
37 *Advanced Research Computing Center, Beartooth Computing Environment, x86_64 cluster*, University of Wyoming, Laramie, WY, 2023.